A physics-informed wave tomography framework for defect reconstruction: a collaborative network scheme

Hairui LIU[1], Qi LI[1], Zhi QIAN[1], Peng LI[1], Zhenghua QIAN[1,✉] , D.Z.LIU[2,✉]

1. *State Key Laboratory of Mechanics and Control for Aerospace Structures, College of Aerospace Engineering, Nanjing University of Aeronautics and Astronautics, Nanjing 210016, China;*
2. *School of Engineering, University of East Anglia, Norwich NR4 7TJ, U. K*

Abstract: It is challenging for guided wave tomography methods to intelligently solve problems in the area of structural defect detection, as this requires more data to achieve the high-accuracy reconstruction of defects. To meet this end, a physics-informed wave tomography framework (PIWT) with a collaborative network scheme is proposed in this paper to reconstruct defects in metal plates with high levels of accuracy and efficiency. First, taking the spatial coordinate information of the point source and sampling points as the inputs of the deep learning collaborative network, a physical principle-based prediction framework is established by minimizing the loss functions to realize the mapping of inputs to outputs, which are represented as the travel time and wave velocity in two collaborative networks for defect reconstruction. To effectively guide the convergence direction of the collaborative network for efficient computations, the waveguide governing equations and boundary conditions are leveraged as the constraints on PIWT to realize the defect reconstruction. As the developed approach belongs to the class of mesh-free methods, its superiority over the conventional mesh-based ultrasonic Lamb wave tomography imaging (ULWTI) technique is demonstrated for defect reconstruction throughout the numerical and experimental examples in terms of accuracy. Moreover, the effects of pre-training on the accelerated convergence and accuracy of the PIWT framework are discussed to allow the training with few epochs and also help effectively achieve real-time high-precision defect reconstruction in the fields of non-destructive testing and structural health monitoring, thus offering a promising solution for broader engineering applications.

Keywords: Guided wave, PINN, Defect reconstruction, Wave tomography, Machine Learning

✉Zhenghua Qian (qianzh@nuaa.edu.cn) and Dianzi Liu (Dianzi.Liu@uea.ac.uk)

1. Introduction

Corrosion of metals is a major issue in industrial production, particularly in regions that would normally be difficult to access using conventional inspection techniques, such as flat plates and pipes. NDT provides a continuous inspection method that enables the detection and localization of defects[1], but accurate estimation of the extent of damage remains a challenge [2].

Guided wave inspection is a popular method for qualitative imaging of corrosion by correlating the current state of the structure with a baseline undamaged state in the baseline method [3]. Commonly used features including time-of-flight (TOF) and peak amplitude envelopes for selected modes [4-6] have been widely used for structural defect detection. Other features including the ratio of the energy distribution between the fundamental symmetric mode S_0 and the first antisymmetric mode A_1[7] and the ratio of S_0 to the fundamental antisymmetric mode A_0[8], have also been paid attention. Usually when these features are obtained, an algorithm is on demand to generate the mappings that graphically depict the region of interest.

Ultrasonic Lamb wave tomography imaging (ULWTI) [9] is a commonly used technique that can image the internal structure of an object without damaging it. Various reconstruction algorithms have been investigated, such as filtered back projection (FBP)[10] and algebraic reconstruction techniques (ART) [11]. As FBP has the disadvantage of large noise and low signal-to-noise ratio, ART is more often used in high-precision image reconstruction. However, ART uses only one ray per iteration, making it less stable and less parallelizable. To address these limitations, the simultaneous algebraic reconstruction technique (SART) [12] and simultaneous iterative reconstruction technique (SIRT) [13] have been developed. These algorithms consider the effects of all rays simultaneously in each iteration, enabling better control of measurement errors and interference factors in the iterative reconstructions. Nevertheless, these methods still face challenges such as the insufficient accuracy and the requirement of initial conditions. Therefore, traditional defect detection methods have difficulties in achieving high-precision reconstruction of defects with limited travel time data, and the reconstruction results heavily rely on the initial model set for iterations.

In recent years, machine learning has become increasingly popular in solving inverse problems such as tomographic imaging [14-16]. Data-driven machine learning algorithms used in these approaches relied on the accuracy of the data, lacking the mining of physical information about the problem itself and resulting in a waste of information. To address this issue, Raissi et al. proposed physics-informed neural networks (PINNs) [17], which used deep neural networks (DNNs) to approximate the target partial differential equations (PDEs) by solving the partial differential term of the PDE using the *automatic differentiation* function (AD) of the neural network. This made PINNs a popular alternative to traditional numerical methods for PDEs [18-20], and also extended the broad applications of PINNs to the study of fluids[21-23], heat transfer [24], and material structures [25]. It was noted that using PINNs to solve the Eikonal equations has been widely utilized in wave propagation. Waheed et al. [26] employed PINNs to solve the Eikonal equations and source point singularities by introducing the factored Eikonal equation into the network. How to speed up computation using migration learning and agent models to provide an efficient orthogonal model for solving the Eikonal equations has likewise been investigated. Smith et al. [27] employed a variety of velocity models and a rigorous sampling method to solve the Eikonal equation using a deep learning method called EikoNet, which used the differentiability of neural networks to compute spatial gradients, while the network satisfied the differential equations in 3D space.

In this study, a physics-informed wave tomography (PIWT) method is proposed by incorporating the governing equations and boundary conditions for reconstructing defects in metal plates by a collaborative network scheme with less data. Meanwhile, a stepwise method for constraining the direction of collaborative network convergence is developed to enable the training result in the close vicinity of the global optimum. A pre-training method is also investigated throughout the numerical examples to further accelerate the collaborative network convergence for computational efficiency. This paper is organized as follows: Section 2 discusses the simplified governing equations, called Eikonal equations, for a two-dimensional plate, as well as the data scaling. In Section 3, the iterative mechanism in solving the slowness matrix using ULWTI is briefly reviewed. Following that, the physics-informed wave tomography framework (PIWT) which stems from the collaborative neural network, is introduced for defect reconstruction. In Section 4, these two methods are compared throughout two typical case studies, and an experimental test is also conducted to demonstrate the feasibility of the developed framework. Finally, the application of the PIWT method for defect reconstruction in metal sheets is discussed in detail. Finally, the conclusions of this study are presented in Section 5.

2. Brief review of the solution to wave equations

The theoretical model describing the propagation of Lamb waves in a plate is based on the frequency domain Helmholtz equation[28], which is formulated as :

$$\left(\nabla^2 + k^2\right) p\left(x, y, \omega\right) = s\left(x, y, \omega\right) \tag{1}$$

where $k\left(x, y, \omega\right) = \omega / c\left(x, y\right)$ denotes the wave number, $c\left(x, y\right)$ represents the wave velocity, ω is the angular frequency, $p\left(x, y, \omega\right)$ describes the scalar displacement field of waves, and $s\left(x, y, \omega\right)$ means the wave source. The solution of Eq.1 is defined as $p = A \times \exp\left(-i\omega T\left(x, y\right)\right)$, in which $T\left(x, y\right)$ is the time delay and *A* is a complex constant. A zero travel time at the source point is defined as the boundary condition. Therefore, the problem governed by Eq.1 can be rewritten as the Eikonal equation below, which is a high-frequency approximation:

$$\begin{gathered} \left(\frac{\partial T}{\partial x}\right)^2 + \left(\frac{\partial T}{\partial y}\right)^2 = \frac{1}{c^2\left(x, y\right)} \\ T\left(x_s, y_s\right) = 0 \end{gathered} \tag{2}$$

The solution to Eq.2 can be considered an extension of the wavefront with the constant phase. In 2D space input, the function *T* provides an approximation of the arrival time of a given wave front at each position. According to the ray theory[29], a decrease in wall thickness of the plate corresponds to a change in the velocity field, which in turn affects the arrival time of Lamb waves.

To circumvent singularities at the point source, the Eikonal equation is modified with multiplicative coefficients by decomposing the unknown scalar displacement field of waves into two components [26] as follows:

$$T\left(x, y\right) = T_0\left(x, y\right) \tau\left(x, y\right) \tag{3}$$

where $T_0\left(x, y\right)$ is the analytical solution defined by：

$$T_0\left(x, y\right) = \frac{\sqrt{\left(x - x_S\right)^2 + \left(y - y_S\right)^2}}{c^2\left(x_S, y_S\right)} \tag{4}$$

Substituting Eq.3 into Eq.2, the final Eikonal equation for solving the forward propagation problem using multiplicative coefficients is derived as follows:

$$T_0^2 |\nabla\tau|^2 + \tau^2 |\nabla T_0|^2 + 2T_0\tau(\nabla T_0.\nabla\tau) = \frac{1}{c^2(x,y)}$$
$$\tau(x_s, y_s) = 1 \tag{5}$$

To reconstruct defects using τ , the velocity mathematical equation should be solved using partial travel time data. The following scaling is performed to amplify the variation of τ by Eq.6:

$$\tau^*(x,y) = \frac{\tau(x,y) - \tau_{\min}}{\tau_{\max} - \tau_{\min}} \tag{6}$$

where the scaling factors $\tau_{\max}$ and $\tau_{\min}$ are determined by numerical experiments, e.g., $\tau_{\max}$ =1.1 and $\tau_{\min}$ = 0.9 in this study. The residual term evaluated by the backpropagation of the collaborative neural network for the determination of parameters is defined by Eq.7:

$$f := T_0^2 |\nabla\tau^*|^2 + \tau^{*2} |\nabla T_0|^2 + 2T_0\tau^*(\nabla T_0.\nabla\tau^*) - \frac{1}{c^2(x,y)}$$
$$h := \tau^*(x_s, y_s) - 1 \tag{7}$$

where $f:$ represents the residual term of the governing equation and $h:$ means the residual term of boundary conditions.

3. The proposed physics-informed wave tomography framework (PIWT)

3.1 Ultrasound Lamb Wave Tomography Imaging (ULWTI) Method

The fundamental concept of ultrasound Lamb wave tomography imaging (ULWTI) method is illustrated in Fig.1. The imaging process involves the deployment of transducers for excitation and reception of waves on opposite sides of the cross-rectangular imaging area in an aluminum plate, which is uniformly partitioned into small grids and each grid serves as a pixel. Within each pixel grid, the thickness and wave velocity of the aluminum plate are assumed to be constant. Thus, the ultimate objective of imaging is transformed to determine the plate's thickness of each pixel grid.

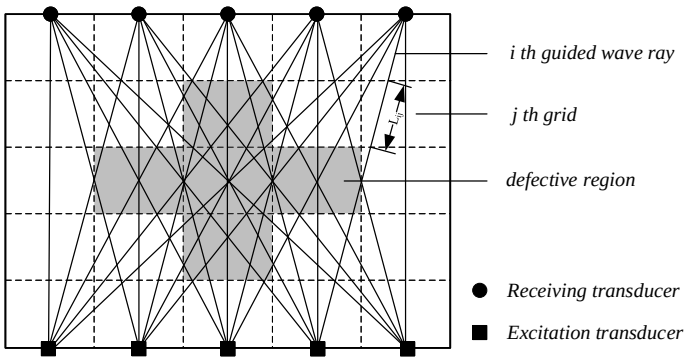

Fig1 Fundamental principles of ULWTI

It is worth noting that the length of the *i*th guided wave ray traveling over the *j*th grid is denoted as L_{ij} , which is an item in the path matrix. Based on the geometric relations, the propagation of a guided wave ray in the structure should satisfy the linear system of equations:

$$T_i = \sum_{j=1}^{M_s \times N_s} L_{ij} \times S_j \quad \left(i = 1, 2, \cdots, P^2\right) \tag{8}$$

where *P* represents the total number of excitation and reception transducers. S_j describes the slowness which is known as the inverse of the velocity.

As this system of simultaneous equations is usually large in dimension, it might be considered underdetermined or overdetermined when iterative methods are adopted for the solution. The commonly used SIRT method[30] has the limitation to efficiently tackle this issue. A neural network-based approach utilizing a single layer of neurons to solve Eq.8 has been supplied in this Section. The path matrix denoted as $\boldsymbol{L}$ serves as the input to the network and the output is the walk time $\boldsymbol{T}$. The network weight is represented by the slowness matrix $\boldsymbol{S}$ of the inspection region, with an associated error $\boldsymbol{\varepsilon} = \hat{\boldsymbol{T}} - \boldsymbol{T}$. The network weight is continually adjusted through error iterations for the minimum loss until the maximum number of iterations is reached or the error $\boldsymbol{\varepsilon}$ is below a specific threshold. In each iteration, the network weighting coefficient $\boldsymbol{S}$ is updated utilizing the following formulation:

$$\boldsymbol{S}^{(k+1)} = \boldsymbol{S}^{(k)} + \eta \boldsymbol{L}^T (\hat{\boldsymbol{T}} - \boldsymbol{T}) \tag{9}$$

where the learning rate η refers to the step size $(0 < \eta \leq 1)$ that adjusts the correction of the weighting coefficients at each iteration.

3.2 The proposed physics informed wave tomography (PIWT)

The collaborative network of PIWT framework is primarily composed of more than one fully connected feedforward neural networks. Fully connected feedforward networks are separately defined, for example, the first network has an input layer consisting of the physical coordinates (x, y) of the received signal point and the source point coordinates (x_s, y_s). Also, the number of hidden layers is denoted as L_1, and the output layer is represented by the normalized travel time coefficients τ to be designed. The second network includes an input layer consisting of the physical coordinates (x, y) of the received signal point only, L_2 hidden layers and an output layer of the wave velocity c. Thus, the partial differential equations defined by Eq.7 are solved by automatic differentiation[31].

Assume that there are N_l neurons in the lth layer of the collaborative network. Thus, a linear transformation is applied to the input $\boldsymbol{x}^{l-1} \in \mathrm{R}^{N_{l-1}}$ in the layer l using a nonlinear activation function σ:

$$H\left(\boldsymbol{x}^{l-1}\right)=\sigma\left(\boldsymbol{w}^{l} \boldsymbol{x}^{l-1}+\boldsymbol{b}^{l}\right)$$

where $H\left(\boldsymbol{x}^{l-1}\right)$ describes the output of the lth layer, $\boldsymbol{w}^{l} \in \mathrm{R}^{N_l \times N_{l-1}}$ and $\boldsymbol{b}^{l} \in \mathrm{R}^{N_l}$ are the item in the matrix of weighting coefficients and the bias vector of the lth layer, respectively. Throughout the successive operations of the collaborative network, the total number of variables in the network is denoted by $\sum_1^l\left(N_l \times N_{l-1}\right)+\boldsymbol{b}^{l}$.

The primary concept of PIWT is to employ a collaborative neural network to approximate unknown solutions to the given PDE described by Eq.5. To incorporate the physical principles of the governing equation and initial conditions into the loss function in the training phase, the loss function of the PIWT collaborative network is formulated as follows:

$$MSE=\lambda_1 MSE_0+\lambda_2 MSE_b+\lambda_3 MSE_f \tag{10}$$

$$MSE_0=\frac{1}{N_0} \sum_{i=1}^{N_0}\left|\hat{\tau}\left(x_0^i, y_0^i\right)-\tau\left(x_0^i, y_0^i\right)\right|^2$$

$$MSE_b=\frac{1}{N_b} \sum_{i=1}^{N_b}\left|\hat{h}\left(x_b^i, y_b^i\right)\right|^2$$

$$MSE_f=\frac{1}{N_f} \sum_{i=1}^{N_f}\left|f\left(x_f^i, y_f^i\right)\right|^2$$

where N_0, N_b, and N_f are the numbers of sampling points in training data, source points and the entire training space, respectively. The labeled coefficients $\tau(x, y)$ representing the travel time in the

training data of the PIWT collaborative network are normalized and denoted as $\left\{x_0^i, y_0^i, \tau^i\right\}_{i=1}^{N_0}$, whereas $\left\{x_b^i, y_b^i\right\}_{i=1}^{N_b}$ represents the coordinates at each training source point corresponding to $h(x, y)$ in Eq.7. Moreover, the randomly sampled training data is represented by $f(x, y)$ and the coordinates over the entire training space are denoted as $\left\{x_f^i, y_f^i\right\}_{i=1}^{N_f}$. The weighting coefficients λ_1, λ_2, and λ_3 in the loss function can be adjusted to accelerate the model convergence and the direction of the convergence.

Two fully connected networks are employed in this study including 40 neurons per layer in three hidden layers, the hyperbolic tangent activation function for the prediction of the travel time coefficient τ and the wave velocity *c*. Some frequently used activation functions are provided in Fig 2. As compared with the other activation functions, the advantage of the hyperbolic tangent activation function lies in its ability to scale input values in a range of -1 and 1, realizing a smooth and symmetric non-linear transformation. This property makes it well-suited for tasks that require the model to learn complex patterns and understand intrinsic relationships among variables. Moreover, the hyperbolic tangent function maintains the differentiability across its entire range, enabling the efficient gradient-based optimization during the training process. The collaborative network architecture of PIWT is shown in Fig.3. To overcome the limitations of sparse datasets and non-smooth objective functions defined in the models during the deep learning process, the network parameters are optimized using the "Adam" optimization algorithm [32] to estimate the first-order and second-order moments of the gradient so that dynamical adjustment of the learning rate for each parameter can be achieved. Also, the collaborative neural networks are trained on NVIDIA GeForce RTX 3050 GPUs.

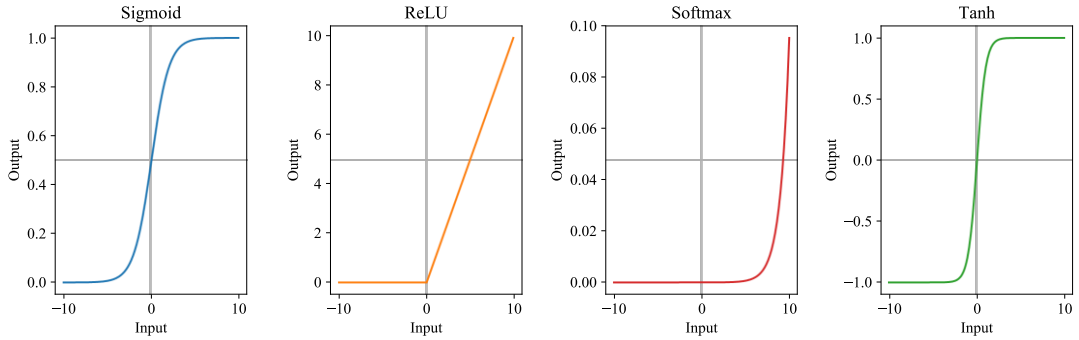

Fig.2 Frequently used activation functions σ in neural networks

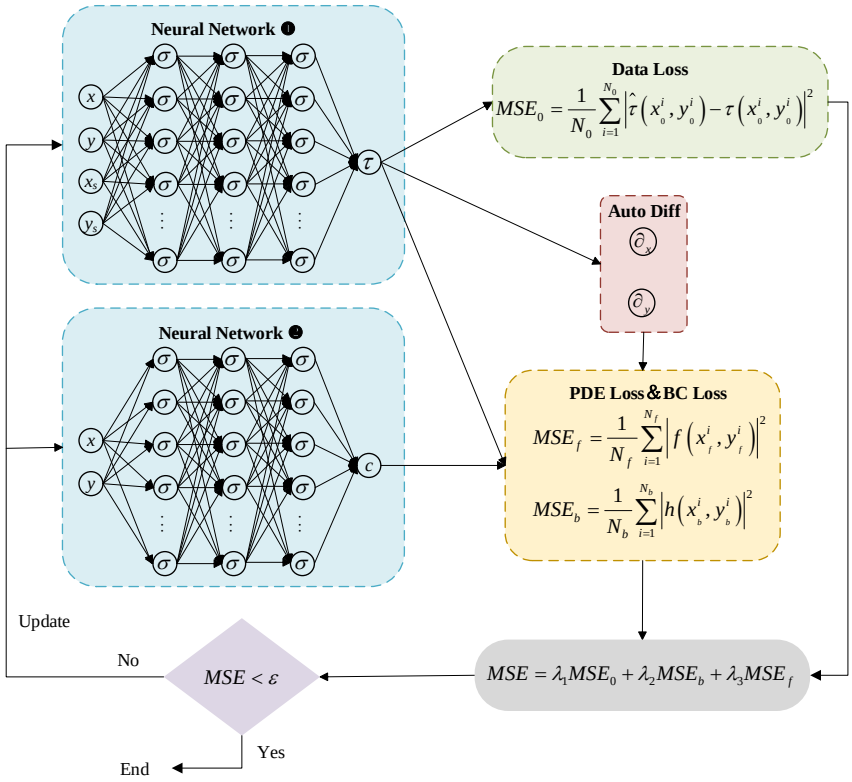

Fig.3 Structural diagram of PIWT framework. Left: Two fully connected neural networks are used to output the travel time coefficient τ and wave velocity c. Right: the loss of data samples with labels MSE_0, the loss of physical control equations MSE_f and the loss of boundary conditions MSE_b.

4. PIWT framework verification by numerical and experimental cases

In this section, results by the proposed PIWT method and the conventional ULWTI method are compared to demonstrate the advantages of the fusion of data-driven deep learning technique and primary wave principles for imaging circular and elliptical defects in metal structures. A python extension module called scikit-fmm[33] that provides an efficient solution to the Eikonal equation using the fast marching method, is employed to conduct numerical simulations for the generation of the travel time data.

4.1 Numerical Example1: Elliptical defect detection

In this section, the imaging of elliptical defects in a 1m×1m metal plate is investigated. Assume that the wave velocities of 1800m/s and 2400m/s propagate in the defect and defect-free areas, respectively. The plate has an elliptical defect with a radius of 0.23 m in the direction of the long axis and 0.15 m in the direction of the short axis. To facilitate defect imaging, a total of 42 receiving transducers that receive signals emitted by probes traveling in opposite directions are uniformly positioned along the upper and

lower boundaries of the plate, as depicted in Fig.4.

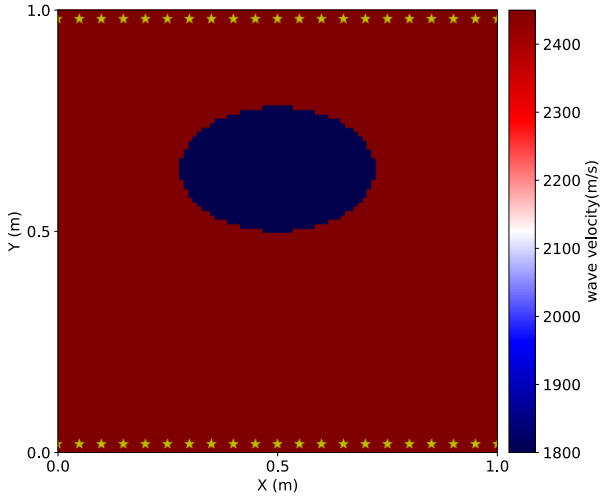

Fig.4 Schematic diagram of the wave velocity of a metal plate containing an elliptical defects: Yellow star dots represent the ultrasonic transducer detection array.

In the conventional ULWTI method, the metal plate is discretized into 100×100 small grids in the *x* and *y* directions. The slowness value of 1/2400 is set for all the network weights during the initialization of the collaborative network to approximate the solution to Eq.8. The collaborative network is trained with the parameters including the maximum iteration number of 20,000, a learning rate of 0.001 and the convergence criterion of $\|\boldsymbol{\varepsilon}\|_1 = 10e-7$.

In the proposed PIWT method, 2500 uniformly distributed points are selected in the *xoy* plane as the training dataset and are denoted as $\left\{x_f^i, y_f^i\right\}_{i=1}^{2500}$. As the data-driven training set, 21×21 sampling points received by the probes are depicted as $\left\{x_0^i, y_0^i, \tau^i\right\}_{i=1}^{441}$, and 42 travel times labeled as the source points in the training dataset are represented by $\left\{x_b^i, y_b^i\right\}_{i=1}^{42}$. The initial learning rate is initially set to 0.01 and then is reduced by half for every 200 training epochs. A stepwise training method for the wave velocity *c* and the traveling time coefficient is developed to effectively constrain the solution space. The working mechanism of the stepwise training method is explained as follows: At the beginning, the network with the labeled data is trained with a fixed value of *c* for 100 epochs. Then, the network is trained with a fixed value of τ for 100 epochs. Repeat the above training process twice before unlocking the parameters of the two networks. Finally, the collaborative network is trained simultaneously for 500 epochs. This stepwise training method enables the results in the training process to approximate the global optimum by leveraging the labeled data. Also, the weighting coefficients in Eq.10 are initialized

to $\lambda_1 = \lambda_2 = 1$ and $\lambda_3 = 0.1$.

In terms of the imaging quality, the ULWTI method produces considerable amount of noise in the background of results shown in Fig.5(a), due to the correlation between the imaging accuracy and the grid precision. Moreover, the increased density of the grid also leads to a noisy background, as insufficient rays pass through certain grids, while the PIWT method is a mesh-free method and its accuracy is independent of the selection scheme of training points. Therefore, PIWT has the ability to generate the results with a cleaner background, which is shown in Figure 5(c).

To detect the accurate localization of defects, the ULWTI method in Figure 5(b) has the limitation to provide a comprehensive location of the defect, as the center of the reconstructed defect is shifted as compared with the results of the benchmark model shown in Table 1. Moreover, the final imaging is dispersed throughout the path of the rays, causing the challenge to detect the profile of the defect. Nevertheless, the proposed PIWT method demonstrates the capability of accurately locating and detecting the defect shown in Figure 5(d). As there is no observable sharp change in gradient at the edges of defects, the PIWT method just conducts automatic differentiation-based calculations which leads to gradients that are asymptotic.

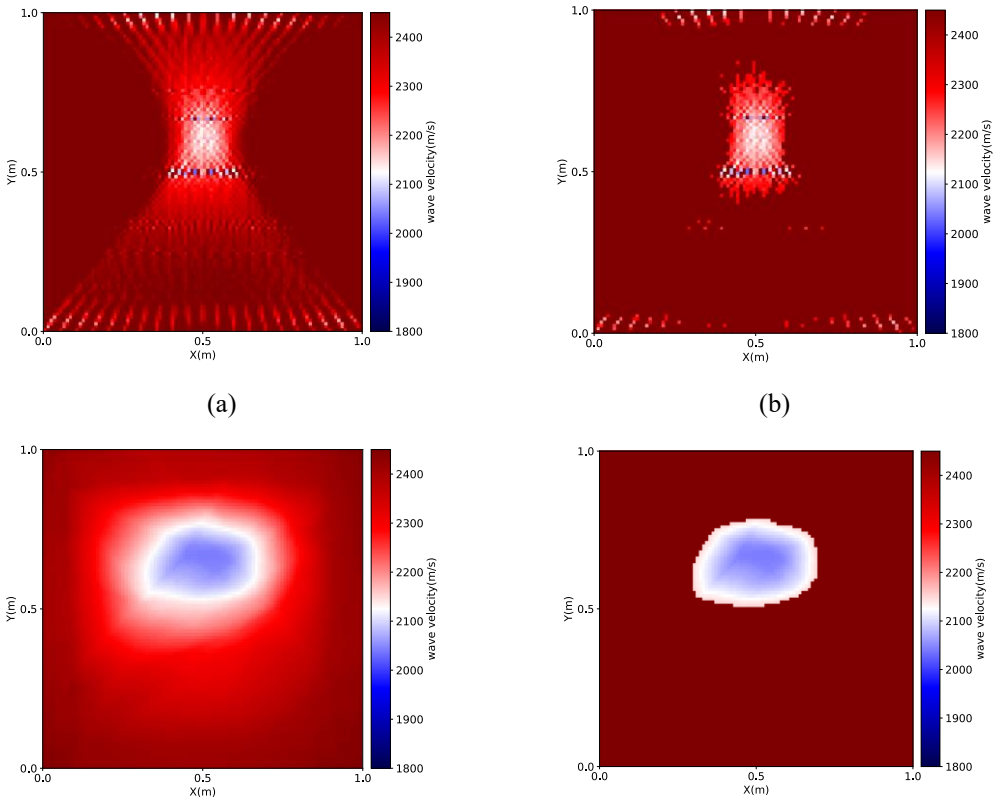

(a) (b)

(c) (d)

Fig.5 Elliptical defect reconstruction by ULWTI (a) and its image filtered by a threshold value(b) ; The reconstruction result by PIWT (c) and the corresponding image filtered by the same threshold value (d).

Table 1 Assessment results of the elliptical defect center and position by different methods.

		ULWTI	PIWT	True
Center	X	0.48	0.53	0.5
position(m)	Y	0.595	0.675	0.64

The wave velocity changes in two directions at the center of the defect are shown in Fig.6 using these two algorithms. PIWT provides more accurate defect size assessment values in both directions from the defect center than ULWT. Therefore, the proposed approach can be implemented as an add-on tool for assessing the change in velocity near the vicinity of the defect location.

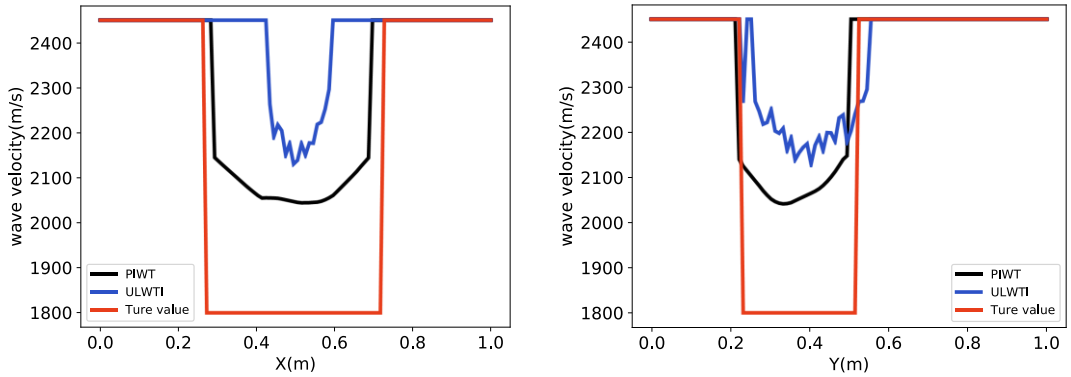

(a) (b)

Fig.6 Comparison of the velocity reconstructions across the defect center along the x-axis (a) and y-axis (b) directions using different detection methods.

4.2 Numerical Example2: Circular defect detection

A case study involving the detection of circular defects is presented to demonstrate the versatility of the proposed PIWT. A metal plate by 1m×1m containing a circular defect with the radius of 0.15m is investigated. Assume that the waves with the velocities of 1800m/s and 2400m/s propagate in the defect and defect-free areas, respectively. The arrangement of transducers are depicted in Fig.7.

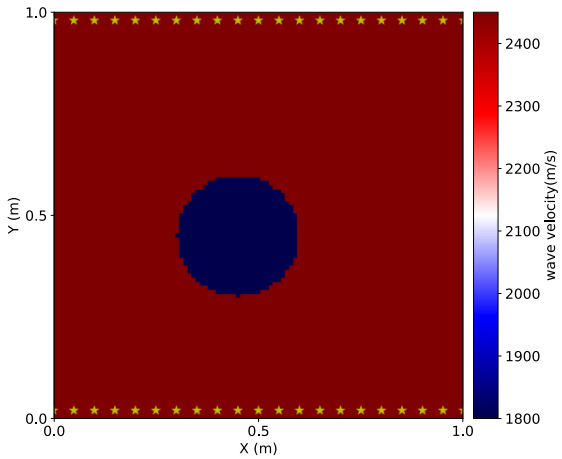

Fig.7 Schematic diagram of the wave velocity of a metal plate containing a circular defect: Yellow star dots represent the ultrasonic transducer detection array.

In Fig.8(a), it is noted that the ULWTI method has the ability to identify the defect area. However, the detection quality is poor and the profile of the defect cannot be clearly imaged. Due to the limited availability of travel time data, the defect profile that can be detected by ULWTI remains indistinguishable, thereby limiting to serve as a reference for defect localization. Nevertheless, the PIWT method has the ability to accurately locate and detect the defect shown in Figure 8(d), as the closely resembling contour of the imaging results is evidenced by a perfect circle. The superiority of the PIWT approach over ULWTI in reconstructing the defect position and size of defects is demonstrated by the image presented in Table 2 and Fig.9.

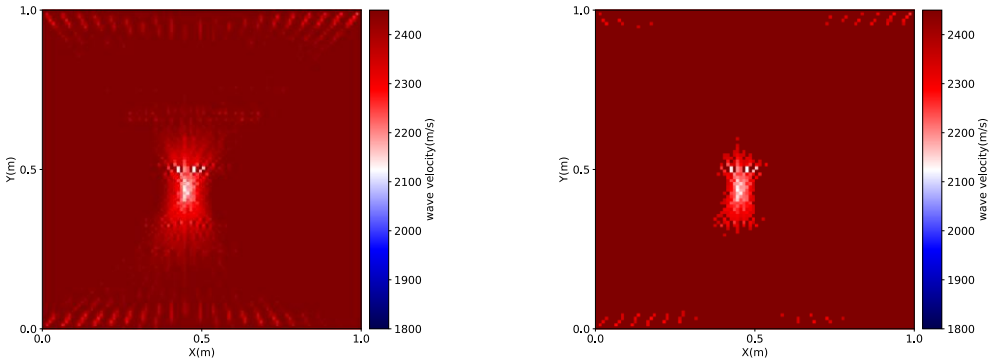

(a) (b)

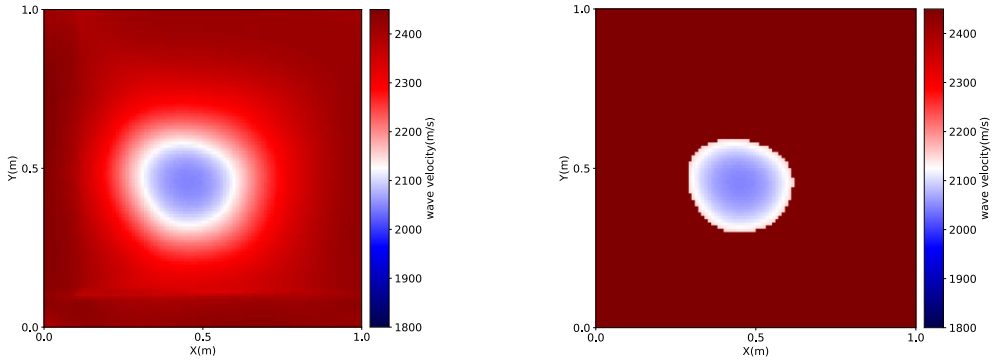

(c) (d)

Fig.8 Circular defect reconstruction by ULWTI (a) and its image filtered by a threshold value(b) ; The reconstruction result by PIWT (c) and the corresponding image filtered by the same threshold value (d).

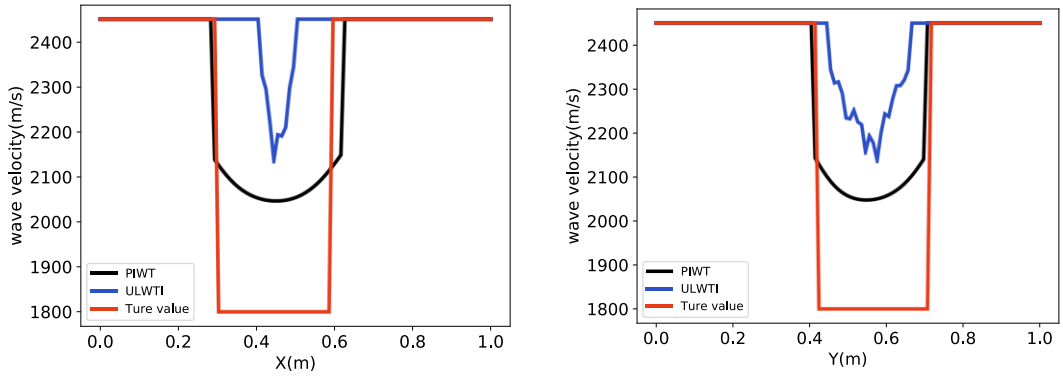

(a) (b)

Fig.9 Comparison of the velocity reconstructions across the defect center along the x-axis (a) and y-axis (b) directions using different detection methods.

Table 2. Assessment results of the circular defect center and position by different methods.

		ULWTI	PIWT	True
Center	X	0.43	0.44	0.45
position(m)	Y	0.52	0.45	0.45

4.3. Experimental validation

To further validate the accuracy and feasibility of the developed PIWT framework and also investigate the impact of the probe quantity on defect reconstructions, an experimental test is designed in Fig.10. In this test, a 2-mm thick elliptical surface defect is fabricated inside a 3-mm thick aluminum plate. Non-contact air-coupled probes (Japan Probe 0.2 K 14 × 20 N) are utilized as transducers, and a non-destructive testing (NDT) system (JPR-600C) is used for both excitation and reception, as shown in

Fig. 10(a). A 5-cycle Hanning-windowed toneburst signal with a central frequency of 200 kHz is generated for incident waves. The experimental data is collected by a square array consisting of 32 ultrasonic probes. Using this array of sensors, a signal is excited by one probe, while the other 31 probes work as receivers. Finally, a dataset in a form of matrix by 32 (number of excitations) × 31 (number of receptions) is obtained.

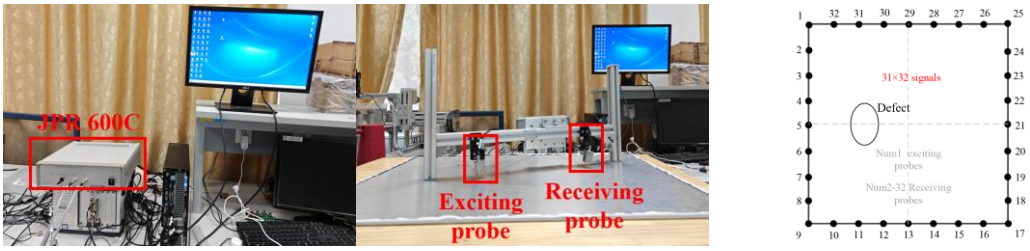

(a) (b)

Fig 10. (a) Experimental platform and transducers. (b) Schematic arrangement of exciting and receiving points.

The signal acquired from the experiments is depicted in Fig. 11(a). Referring to the relationship between the velocity and Frequency-Thickness shown in Fig. 1, the wave packet corresponding to the A0 mode in Fig. 11(a) is identified. Subsequent wavelet transformation yields the corresponding result reflecting the relationship between the energy density and time, as shown in Figure 11(b). It is worth noting that after extracting the signal travel time from Fig.11(b), it is necessary to subtract the time taken by the guided wave propagating from the air-coupled excitation source through the air to the metal plate.

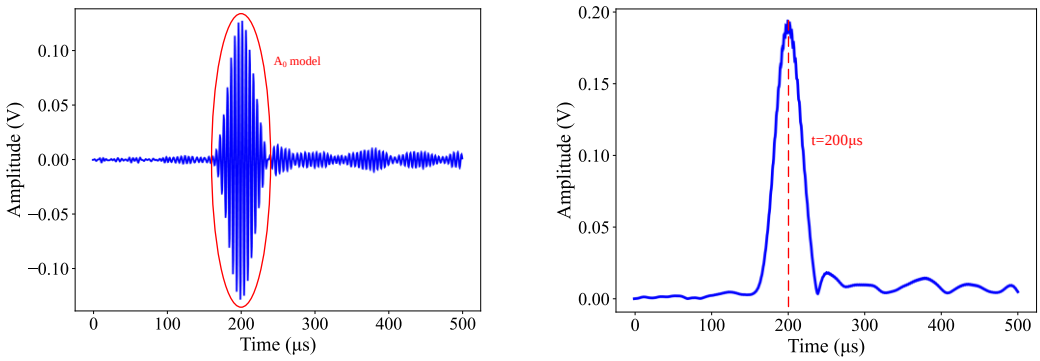

(a) (b)

Fig.11 Experimental signal corresponding to the excitation frequency of 200 kHz: (a) the original signal; (b) the signal processed by continuous wave transformation (CWT)

Due to the constraints imposed on the probe size, it is not feasible to arrange an excessive number of sensors along a single edge of the experimental plate. To ensure the experimental accuracy, sensors are strategically positioned along all four edges of the defective plate. Applying the specified threshold,

the resulting image is shown in Fig. 12(a). The changes in thickness along the x- and y-axes are presented in Fig. 12(b) and 12(c), respectively. The actual center of the defect is located at (9 cm, 20.0 cm), while the reconstructed center is at (9.6 cm, 19.6 cm), indicating the minimal discrepancy of defect location. Moreover, the elliptical defect reconstruction appears wider along the short axis as compared to the actual defect dimension. This can be attributed to the off-center positioning, as such misalignment likely leads to fewer ultrasonic rays passing through the defect, thereby causing the observed deviation.

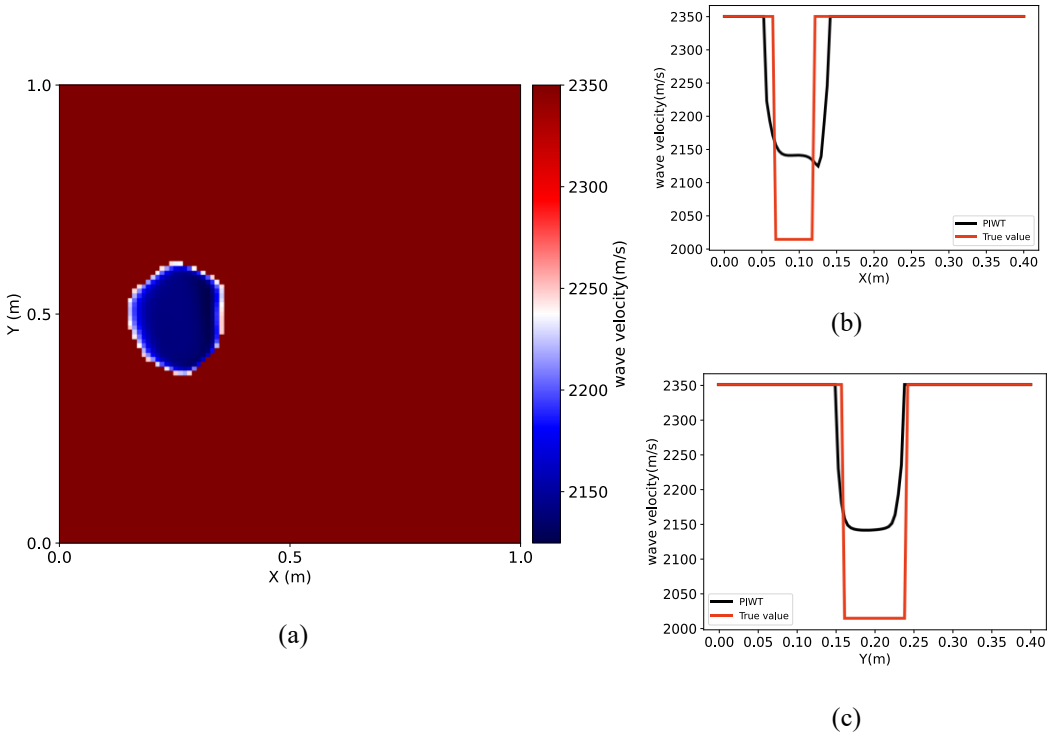

Fig 12. (a)Final imaging experiment result after applying threshold, reconstruction of the velocity at the defect center along the x-axis (a) and y-axis (b) from experimental data.

4.4. Pre-training strategy

Though the proposed PIWT offers the superior accuracy and imaging quality as compared with the results by ULWTI, its computational efficiency should be improved. To address this issue, the pre-training strategy, which has been commonly used in deep learning [34], is developed in this study. Parameters of the collaborative neural networks are pre-trained using data from other defect inversion tasks to initialize the weight matrix $\boldsymbol{w}$ and bias vector $\boldsymbol{b}$. With the implementation of the pre-training strategy, the number of required training epochs can be reduced effectively. This is demonstrated by the comparison results of the convergence rate of loss function in Fig.13. The pre-trained model with the

learned physical knowledge exhibits a lower initial loss and faster convergence as compared with the results by the non-pretrained model. Furthermore, the pre-trained model has the capability of defect predictions with a higher accuracy after 300 epochs of training, indicating that the PIWT model with the implemented pre-training strategy can significantly improve the convergence rate and accuracy. The reconstructed defect is much closer to the ground values in Figure 14. Therefore, the pre-training strategy implemented into PIWT significantly reduces the training time and improves the detection accuracy.

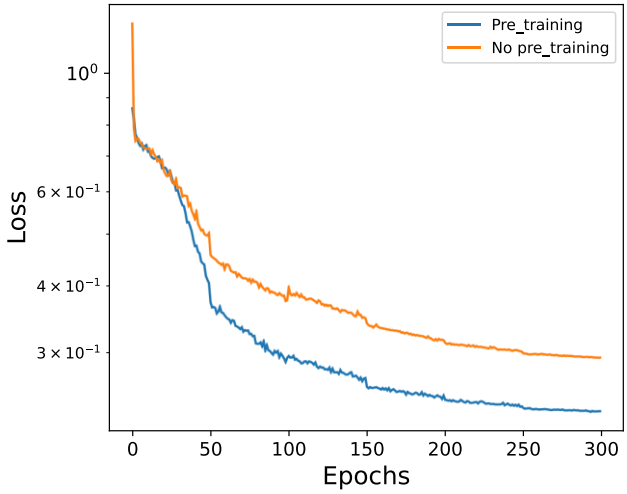

Fig.13 Comparison of Loss convergence using PIWT with and Without Pre-Training.

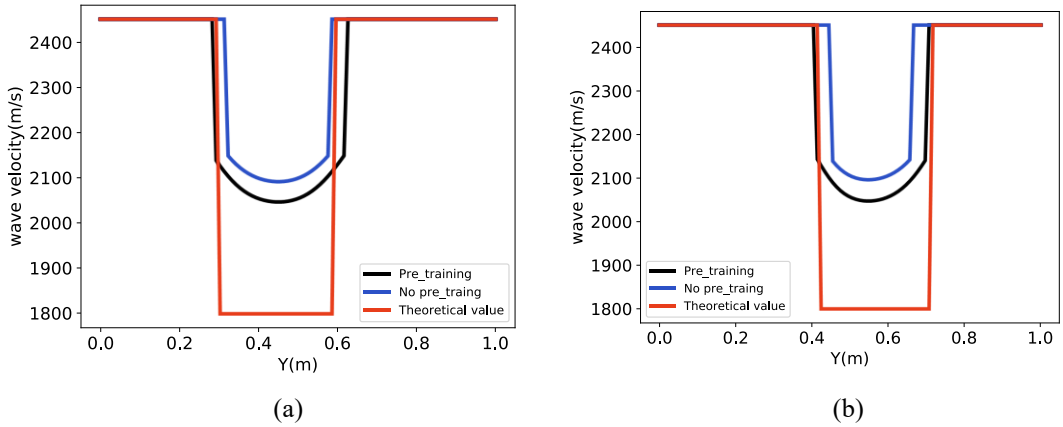

Fig.14 Comparison of the velocity reconstructions across the defect center along the x-axis (a) and y-axis (b) directions with and without pretraining strategy: a cross-section point of view

4.5 Discussion

The simulation results demonstrate that the proposed PIWT framework, an independent and efficient technique, has the ability to realize tomographic imaging inversion of defects in metal plates with high levels of accuracy and robustness as compared with the results by the conventional ULWTI

method. Remarkably, even with limited data, the PIWT framework consisting a collaborative neural network can also enable the global optimal solution by incorporating the waveguide governing equations and boundary conditions as the constraints, thus providing a novel and powerful approach to tomographic imaging applicable to various engineering subjects.

The developed pre-training strategy is incorporated to expedite the solution efficiency of PIWT in this paper whereby the target collaborative network parameters are initialized with collaborative network parameters trained on other defect types. Such an initialized model has already acquired some level of physical knowledge, enabling faster training and reduction in computational costs. Furthermore, as it captures common features and patterns shared by defects, the pre-training strategy implemented into PIWT enhances the model's generalization capacity[34], leading to the superior performance in the process of new defects.

Though PIWT shows promising results, there are still some challenges to be addressed. One of the challenges is to use automatic differentiation of neural networks to represent the partial differential term in solving the physical equations. This results in the edges of the original defect model potentially becoming blurred, as the automatic differentiation function lacks to effectively realize the sharp changes in the gradient of the edges. Even the method is able to accurately image defects, it still has difficulty to accurately reconstruct the wave velocity in the vicinity of the defect. In future work, more complex arrays of ultrasonic transducers will be used to tackle this problem. Another challenge is related to the computational time. Although the pre-training strategy has been introduced to improve the computational efficiency, it still has much space to be further adapted for the broader practical tomographic applications. It should be noted that with the rapid development of computer technology, the use of GPU for parallel computing may offer a promising solution to this challenge[35].

5. Conclusion

In this study, a mesh-free physics-informed wave tomography framework (PIWT) framework for defect reconstruction is proposed to employ a collaborative network for the outputs by the governing equations and boundary conditions, respectively. Furthermore, a stepwise training strategy is adopted to ultimately lead to the greater collaborative network stability by constraining the solution space. Throughout various defect examples by comparison of the reconstruction results between PIWT and the

traditional ULWTI, it is demonstrated that the PIWT has superior performances including effectiveness, accuracy and robustness for the reconstruction of defects in metal plates. Results show that the average prediction accuracy for the center location of random defects by PIWT is reduced by less than 6% and for defect sizes is less than 15% lower, as compared to the reference defects, demonstrating the great generalization of the developed PIWT framework and its feasibility on practical applications. Therefore, it is a high-precision quantitative defect reconstruction technique in comparison with the conventional ULWTI method. Furthermore, this paper investigates the impact of the pre-training strategy on PIWT. The developed pre-training strategy accelerates the collaborative network convergence and also improves accuracy, thus providing a promising and versatile defect reconstruction method in the field of non-destructive testing. Summarily, results presented in this study strongly suggest that PIWT, the synergy of deep learning and physical principles, has the potential to and also provides the insight into the development of a robust technology for continuous monitoring of corrosion and erosion damages in plates with high levels of accuracy and reliability.

Acknowledgements: Postgraduate Research & Practice Innovation Program of Jiangsu Province.

References

[1] Huthwaite P, Simonetti F (2013) High-resolution guided wave tomography. Wave Motion 50: 979-993.

[2] Brath A J, Simonetti F, Nagy P B et al (2014) Acoustic formulation of elastic guided wave propagation and scattering in curved tubular structures. IEEE Transactions on Ultrasonics, Ferroelectrics, and Frequency Control 61: 815-829.

[3] Lu Y, Michaels J E (2005) A methodology for structural health monitoring with diffuse ultrasonic waves in the presence of temperature variations. Ultrasonics 43: 717-731.

[4] Pei J, Yousuf M I, Degertekin F L et al (1996) Lamb wave tomography and its application in pipe erosion/corrosion monitoring. Journal of Research in Nondestructive Evaluation 8: 189-197.

[5] Croxford A J, Wilcox P D, Drinkwater B W et al (2007) Strategies for guided-wave structural health monitoring. Proceedings of the Royal Society A: Mathematical, Physical and Engineering Sciences 463: 2961-2981.

[6] Ostachowicz W, Kudela P, Malinowski P et al (2009) Damage localisation in plate-like structures based on PZT sensors. Mechanical Systems and Signal Processing 23: 1805-1829.

[7] Hua J, Cao X, Yi Y et al (2020) Time-frequency damage index of Broadband Lamb wave for corrosion inspection. Journal of Sound and Vibration 464: 114985.

[8] Dubuc B, Ebrahimkhanlou A, Livadiotis S et al (2019) Inversion algorithm for Lamb-wave-based depth characterization of acoustic emission sources in plate-like structures. Ultrasonics 99: 105975.

[9] Huang S, Wei Z, Zhao W et al (2014) A new omni-directional EMAT for ultrasonic Lamb wave tomography imaging of metallic plate defects. Sensors 14: 3458-3476.

[10] Zhao X, Royer R L, Owens S E et al (2011) Ultrasonic Lamb wave tomography in structural health monitoring. Smart Materials and Structures 20: 105002.

[11] Livadiotis S, Ebrahimkhanlou A, Salamone S (2019) A helical-based ultrasonic imaging algorithm for structural health monitoring of cylindrical structures. Health Monitoring of Structural and Biological Systems XIII. SPIE, 10972: 8-14.

[12] Andersen A H, Kak A C (1984) Simultaneous algebraic reconstruction technique (SART): a superior implementation of the ART algorithm. Ultrasonic imaging 6: 81-94.

[13] Trampert J, Leveque J J (1990) Simultaneous iterative reconstruction technique: Physical interpretation based on the generalized least squares solution. Journal of Geophysical Research:

Solid Earth 95: 12553-12559.

[14] Würfl T, Ghesu F C, Christlein V et al (2016) Deep learning computed tomography. Medical Image Computing and Computer-Assisted Intervention-MICCAI 2016: 19th International Conference, Athens, Greece, October 17-21, 2016, Proceedings, Part III 19. Springer International Publishing: 432-440.

[15] Araya-Polo M, Jennings J, Adler A et al (2018) Deep-learning tomography. The Leading Edge 37: 58-66.

[16] Wang G, Ye J C, De Man B (2020) Deep learning for tomographic image reconstruction. Nature Machine Intelligence 2: 737-748.

[17] Raissi M, Perdikaris P, Karniadakis G E (2019) Physics-informed neural networks: A deep learning framework for solving forward and inverse problems involving nonlinear partial differential equations. Journal of Computational Physics 378:686–707.

[18] Raissi M (2018) Forward-backward stochastic neural networks: Deep learning of high-dimensional partial differential equations. arXiv preprint arXiv:1804.07010.

[19] Wight C L, Zhao J (2020) Solving allen-cahn and cahn-hilliard equations using the adaptive physics informed neural networks. arXiv preprint arXiv:2007.04542.

[20] Wang S, Yu X, Perdikaris P (2020) When and why pinns fail to train: A neural tangent kernel perspective. arXiv preprint arXiv:2007.14527, 2020.

[21] Molnar J P, Grauer S J (2022) Flow field tomography with uncertainty quantification using a Bayesian physics-informed neural network. Measurement Science and Technology 33(6): 065305.

[22] Cai S, Mao Z, Wang Z et al (2021) Physics-informed neural networks (PINNs) for fluid mechanics: A review. Acta Mechanica Sinica 37: 1727-1738.

[23] Mao Z, Jagtap A D, Karniadakis G E (2020) Physics-informed neural networks for high-speed flows. Computer Methods in Applied Mechanics and Engineering 360: 112789.

[24] Cai S, Wang Z, Wang S et al (2021) Physics-informed neural networks for heat transfer problems. Journal of Heat Transfer 143.

[25] Zhang E, Dao M, Karniadakis G E et al (2022) Analyses of internal structures and defects in materials using physics-informed neural networks. Science Advances 8: eabk0644.

[26] bin Waheed U, Haghighat E, Alkhalifah T et al (2021) PINNeik: Eikonal solution using physics-informed neural networks. Computers & Geosciences 155: 104833.

[27] Smith J D, Azizzadenesheli K, Ross Z E (2020) Eikonet: Solving the eikonal equation with deep neural networks. IEEE Transactions on Geoscience and Remote Sensing 59: 10685-10696.

[28] Huang X, Greenhalgh S (2021) A finite-difference iterative solver of the Helmholtz equation for frequency-domain seismic wave modeling and full-waveform inversionIterative Helmholtz solver. Geophysics 86(2): T107-T116.

[29] Cui H, Li B, Zhou L B et al (2022) Damage detection in thick plate structures based on ultrasonic SH wave. Smart Materials and Structures 31: 095018.

[30] Chen X, Hu H L, Gao C X, et al (2011) Comparison of Algebraic Reconstruction Technique and Simultaneous Iterative Reconstruction Technique in Electrical Capacitance Tomography Image Reconstruction. Journal of Xi'an Jiaotong University 45:25-29.

[31] Abadi M, Barham P, Chen J, et al (2016) Tensorflow: a system for large-scale machine learning. Osdi 16: 265-283.

[32] Kingma D P, Ba J L (2014) “Adam: A method for stochastic optimization,” arXiv preprint arXiv:1412.6980.

[33] the scikit-fmm team (2021) scikit-fmm, a CPU toolkit to formulate the travel time. https://pythonhosted.org/scikit-fmm/, Last accessed on 2021-7-8.

[34] Erhan D, Courville A, Bengio Y, et al (2010) Why does unsupervised pre-training help deep learning?. Proceedings of the thirteenth international conference on artificial intelligence and statistics. JMLR Workshop and Conference Proceedings: 201-208.

[35] Oh K S, Jung K (2004) GPU implementation of neural networks. Pattern Recognition 37: 1311-1314.